

## The MITC4+ shell element in geometric nonlinear analysis

Yeongbin Ko<sup>a</sup>, Phill-Seung Lee<sup>a,\*</sup>, Klaus-Jürgen Bathe<sup>b</sup>

<sup>a</sup> Department of Mechanical Engineering, Korea Advanced Institute of Science and Technology, 291 Daehak-ro, Yuseong-gu, Daejeon 34141, Republic of Korea

<sup>b</sup> Department of Mechanical Engineering, Massachusetts Institute of Technology, Cambridge, MA 02139, USA



### ARTICLE INFO

#### Article history:

Received 27 December 2016

Accepted 27 January 2017

#### Keywords:

Shell structures

4-node shell finite elements

MITC method

Large displacements and rotations

Shear and membrane locking

Reliability in geometric nonlinear analysis

### ABSTRACT

We present the large displacement and rotation formulation of the new MITC4+ shell finite element recently proposed by Ko, Lee and Bathe for linear analysis (Ko et al., 2017) and demonstrate the performance in geometric nonlinear analysis. The element shows in linear analysis an almost ideal convergence behavior since shear and membrane locking is alleviated using the MITC approach. We show now that using the total Lagrangian formulation for large displacements and large rotations, the element is also robust and efficient in nonlinear analysis. We demonstrate the element performance through the solutions of various benchmark problems and reach the important conclusion that the MITC4+ shell element performs reliably and well even when the mesh undergoes large displacements and significant distortions during the response.

© 2017 Elsevier Ltd. All rights reserved.

## 1. Introduction

For the analysis of shell structures, developing “ideal” shell finite elements that satisfy the ellipticity, consistency and inf-sup conditions has been of great interest [1–10]. Such shell elements should pass the basic tests (the isotropy, zero energy mode and patch tests), show uniformly optimal convergence behavior in any shell problem irrespective of the shell geometry, loading and boundary conditions, and do so when regular and even distorted meshes are used [7–10]. Also, the shell elements need to perform equally well in geometric nonlinear analysis where an effective behavior in the nonlinear response predictions is important [4].

In geometric nonlinear analysis of shell structures, significant mesh distortions can occur as the geometry of the elements changes during the response [11–15]. These element geometric changes can lead to locking in bending-dominated shell problems [4,8], that is, an overly stiff behavior of the shell discretization is seen, which can be particularly severe when 4-node shell elements are used to model thin shell structures [1,2,4,8]. Hence, in geometric nonlinear analysis, locking due to the discretization undergoing large displacements can lead to erroneous predictions of load-displacement trajectories and critical loads.

The MITC (Mixed Interpolation of Tensorial Components) method [1–4,16–25] has been used effectively to remedy shear and membrane locking. The classical 4-node MITC shell element (labeled as MITC4 element) has been widely used in practice for

both linear and nonlinear analyses. However, in the original formulation of the MITC4 shell element, membrane locking was not treated, and thus solution accuracy can deteriorate when curved geometries are modeled with distorted meshes [1,2]. Following various attempts to alleviate membrane locking of 4-node shell elements [26–28], we recently presented the new MITC4+ shell element for general linear analysis [1]. This element satisfies all the basic element tests, contains no parameter to adjust, and shows an almost optimal convergence behavior in the solutions of a ‘behavior-encompassing’ set of benchmark problems using regular and distorted meshes. The fact that the element performance is also very good in highly distorted meshes is particularly noteworthy and makes this element an excellent candidate for general large displacement and rotation nonlinear analysis.

This expectation is reasonable because our experience is that if a well-formulated MITC element has been established for linear analysis, then this element formulation can directly be extended to geometric nonlinear analysis without introducing instabilities in the element, like seen in formulations based on incompatible modes and enhanced assumed strains [4,29,30]. In addition, the incompatible modes and enhanced assumed strain elements are computationally more expensive.

In this paper, we present the geometric nonlinear formulation of the new MITC4+ shell. We develop the assumed shear and membrane fields of the element for the total Lagrangian formulation using the Green-Lagrange strains and incremental Green-Lagrange strains to obtain the tangent stiffness matrix and internal force vector [4]. We demonstrate the performance of the element in geometric nonlinear solutions by solving various shell problems

\* Corresponding author.

E-mail address: [phillseung@kaist.edu](mailto:phillseung@kaist.edu) (P.-S. Lee).

with uniform and distorted meshes. To assess the accuracy of the solutions, we compare the predicted response with analytical data and finite element solutions obtained using the MITC4 and MITC9 shell elements. An important conclusion is that the new MITC4+ shell element performs well even when a mesh undergoes significant displacements that could induce some locking, like might be seen in solutions using the classical MITC4 shell element.

## 2. Geometric nonlinear formulation

In this section, we present the geometric nonlinear formulation of the MITC4+ shell element. In the total Lagrangian formulation, the left superscript  $t$  denotes “time” for a general analysis (in static solutions “time” simply denotes the load step and configuration) and the left subscript 0 is used to denote the initial (reference) configuration [4].

### 2.1. Geometry and displacement interpolations

The geometry of the MITC4+ shell element in the configuration at time  $t$  shown in Fig. 1 is interpolated using [1,2]

$$\begin{aligned} {}^t\mathbf{x}(r,s,\zeta) &= {}^t\mathbf{x}_m + \zeta {}^t\mathbf{x}_b \quad \text{with } {}^t\mathbf{x}_m = \sum_{i=1}^4 h_i(r,s) {}^t\mathbf{x}_i \quad \text{and} \\ {}^t\mathbf{x}_b &= \frac{1}{2} \sum_{i=1}^4 a_i h_i(r,s) {}^t\mathbf{V}_n^i, \end{aligned} \quad (1)$$

where  $h_i(r,s)$  is the two-dimensional interpolation function of the standard isoparametric procedure corresponding to node  $i$ ,  ${}^t\mathbf{x}_i$  is the position vector of node  $i$ , and  $a_i$  and  ${}^t\mathbf{V}_n^i$  denote the shell thickness and the director vector at the node, see Fig. 1.

The following representation of interpolation function  $h_i(r,s)$  is useful in the element formulation:

$$h_i(r,s) = \frac{1}{4} (1 + \xi_i r)(1 + \eta_i s) \quad \text{with } i = 1, 2, 3, 4,$$

$$\begin{bmatrix} \xi_1 & \xi_2 & \xi_3 & \xi_4 \end{bmatrix} = \begin{bmatrix} 1 & -1 & -1 & 1 \end{bmatrix}, \quad \begin{bmatrix} \eta_1 & \eta_2 & \eta_3 & \eta_4 \end{bmatrix} = \begin{bmatrix} 1 & 1 & -1 & -1 \end{bmatrix}, \quad (2)$$

in which  $\xi_i$  and  $\eta_i$  are permuted together.

The incremental displacement vector  $\mathbf{u}$  from the configuration at time  $t$  to the configuration at time  $t + \Delta t$  is

$$\mathbf{u}(r,s,\zeta) = {}^{t+\Delta t}\mathbf{x}(r,s,\zeta) - {}^t\mathbf{x}(r,s,\zeta). \quad (3)$$

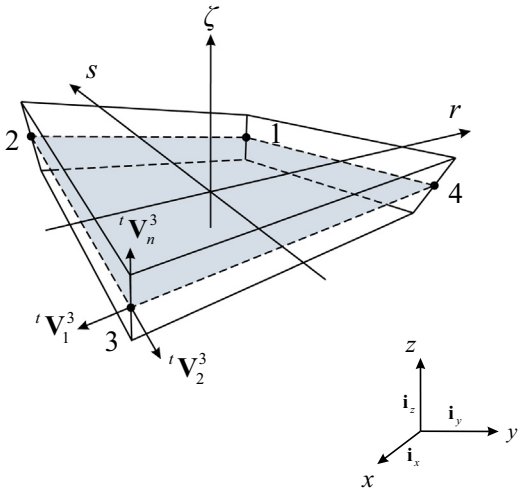


Fig. 1. A standard 4-node quadrilateral continuum mechanics based shell finite element in the configuration at time  $t$ .

Using Eq. (1) in Eq. (3), we obtain

$$\mathbf{u} = \sum_{i=1}^4 h_i(r,s)({}^{t+\Delta t}\mathbf{x}_i - {}^t\mathbf{x}_i) + \frac{\zeta}{2} \sum_{i=1}^4 a_i h_i(r,s)({}^{t+\Delta t}\mathbf{V}_n^i - {}^t\mathbf{V}_n^i), \quad (4a)$$

with

$${}^{t+\Delta t}\mathbf{x}_i - {}^t\mathbf{x}_i = u_i \mathbf{i}_x + v_i \mathbf{i}_y + w_i \mathbf{i}_z, \quad (4b)$$

and to quadratic order

$${}^{t+\Delta t}\mathbf{V}_n^i - {}^t\mathbf{V}_n^i = \mathbf{0}_i \times {}^t\mathbf{V}_n^i + \frac{1}{2} \mathbf{0}_i \times (\mathbf{0}_i \times {}^t\mathbf{V}_n^i), \quad \mathbf{0}_i = {}^t\mathbf{V}_1^i \alpha_i + {}^t\mathbf{V}_2^i \beta_i, \quad (4c)$$

in which  $\mathbf{i}_x$ ,  $\mathbf{i}_y$  and  $\mathbf{i}_z$  are the base vectors of the global Cartesian coordinate system, and at node  $i$ ,  $u_i$ ,  $v_i$  and  $w_i$  are the corresponding displacement components,  ${}^t\mathbf{V}_1^i$  and  ${}^t\mathbf{V}_2^i$  are unit vectors orthogonal to the director vector ( ${}^t\mathbf{V}_n^i$ ) and to each other, and  $\alpha_i$  and  $\beta_i$  denote the rotations of the director vector about  ${}^t\mathbf{V}_1^i$  and  ${}^t\mathbf{V}_2^i$ , respectively [4].

Substituting from Eqs. (4b) and (4c) into Eq. (4a), the incremental displacement is obtained as

$$\mathbf{u}(r,s,\zeta) = \mathbf{u}_m + \zeta(\mathbf{u}_{b1} + \mathbf{u}_{b2}), \quad (5a)$$

where

$$\mathbf{u}_m = \sum_{i=1}^4 h_i(r,s) \mathbf{u}_i, \quad (5b)$$

$$\mathbf{u}_{b1} = \frac{1}{2} \sum_{i=1}^4 a_i h_i(r,s) (-{}^t\mathbf{V}_2^i \alpha_i + {}^t\mathbf{V}_1^i \beta_i), \quad \mathbf{u}_{b2} = -\frac{1}{4} \sum_{i=1}^4 a_i h_i(r,s) (\alpha_i^2 + \beta_i^2) {}^t\mathbf{V}_n^i. \quad (5c)$$

We next group the displacement terms in Eq. (5) as

$$\mathbf{u}_1 = \mathbf{u}_m + \zeta \mathbf{u}_{b1}, \quad \mathbf{u}_2 = \zeta \mathbf{u}_{b2}, \quad (6)$$

where  $\mathbf{u}_1$  and  $\mathbf{u}_2$  contain the linear and quadratic terms of unknown displacements and rotations, respectively.

### 2.2. Green-Lagrange strains

The covariant Green-Lagrange strain components in the configuration at time  $t$  with respect to the reference configuration at time 0 are defined by

$${}^t \varepsilon_{ij}(r,s,\zeta) = \frac{1}{2} ({}^t \mathbf{g}_i \cdot {}^t \mathbf{g}_j - {}^0 \mathbf{g}_i \cdot {}^0 \mathbf{g}_j), \quad (7)$$

in which  ${}^t \mathbf{g}_i = \frac{\partial {}^t \mathbf{x}}{\partial r_i}$  are covariant base vectors with  $r_1 = r$ ,  $r_2 = s$ ,  $r_3 = \zeta$ .

Using Eq. (3) in Eq. (7) applied at time  $t$  and  $t + \Delta t$ , the incremental covariant strain components are

$${}^0 \varepsilon_{ij}(r,s,\zeta) = {}^{t+\Delta t} \varepsilon_{ij}(r,s,\zeta) - {}^t \varepsilon_{ij}(r,s,\zeta) = \frac{1}{2} ({}^t \mathbf{g}_i \cdot \mathbf{u}_j + \mathbf{u}_{i,j} \cdot {}^t \mathbf{g}_j + \mathbf{u}_{i,j} \cdot \mathbf{u}_j), \quad (8)$$

with  $\mathbf{u}_{i,j} = \frac{\partial \mathbf{u}_i}{\partial r_j}$ .

Substituting from Eq. (6) into Eq. (8) and retaining only the strain terms up to second order of unknowns, the incremental strain components can be written as

$${}^0 \varepsilon_{ij}(r,s,\zeta) = {}^0 \varepsilon_{ij}(r,s,\zeta) + {}^0 \eta_{ij}(r,s,\zeta), \quad (9)$$

with

$${}^0 \varepsilon_{ij}(r,s,\zeta) = \frac{1}{2} ({}^t \mathbf{g}_i \cdot \mathbf{u}_{1,j} + \mathbf{u}_{1,i} \cdot {}^t \mathbf{g}_j),$$

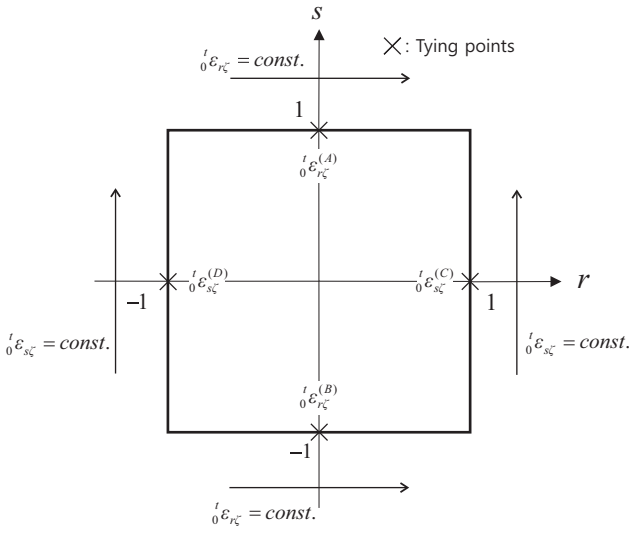


**Fig. 2.** Tying positions (A), (B), (C) and (D) for the assumed transverse shear strain field of the MITC4 shell element. The constant transverse shear strain conditions are imposed along its edges.

$$\eta_{ij}(r, s, \zeta) = \frac{1}{2} (\mathbf{u}_{1,i} \cdot \mathbf{u}_{1,j} + {}^t \mathbf{g}_i \cdot \mathbf{u}_{2,j} + \mathbf{u}_{2,i} \cdot {}^t \mathbf{g}_j) \quad \text{with}$$

$$\mathbf{u}_{1,i} = \frac{\partial \mathbf{u}_1}{\partial r_i}, \quad \mathbf{u}_{2,i} = \frac{\partial \mathbf{u}_2}{\partial r_i},$$

where  $\eta_{ij}$  and  $\eta_{ij}$  are the linear and nonlinear parts, respectively [4,31].

### 2.3. Assumed Green-Lagrange strains

To alleviate shear locking, the assumed transverse shear strains of the classical MITC4 shell element are used [2]

$$\begin{aligned} {}^t \tilde{\epsilon}_{r\zeta} &= \frac{1}{2} (1+s) {}^t \tilde{\epsilon}_{r\zeta}^{(A)} + \frac{1}{2} (1-s) {}^t \tilde{\epsilon}_{r\zeta}^{(B)}, \\ {}^t \tilde{\epsilon}_{s\zeta} &= \frac{1}{2} (1+r) {}^t \tilde{\epsilon}_{s\zeta}^{(C)} + \frac{1}{2} (1-r) {}^t \tilde{\epsilon}_{s\zeta}^{(D)}, \end{aligned} \quad (10)$$

where the tying positions (A), (B), (C) and (D) are shown in Fig. 2 [1,2,8].

In order to alleviate membrane locking, we separate the corresponding membrane strains from the in-plane strains. The covariant in-plane strains in Eq. (7) are expressed as

$${}^t \epsilon_{ij} = {}^t \epsilon_{ij}^m + \zeta {}^t \epsilon_{ij}^{b1} + \zeta^2 {}^t \epsilon_{ij}^{b2} \quad \text{with } i, j = 1, 2, \quad (11a)$$

in which

$${}^t \epsilon_{ij}^m = \frac{1}{2} ({}^t \mathbf{x}_{m,i} \cdot {}^t \mathbf{x}_{m,j} + {}^t \mathbf{x}_{m,j} \cdot {}^t \mathbf{x}_{m,i}) - \frac{1}{2} ({}^0 \mathbf{x}_{m,i} \cdot {}^0 \mathbf{x}_{m,j} + {}^0 \mathbf{x}_{m,j} \cdot {}^0 \mathbf{x}_{m,i}), \quad (11b)$$

$${}^t \epsilon_{ij}^{b1} = ({}^t \mathbf{x}_{m,i} \cdot {}^t \mathbf{x}_{b,j} + {}^t \mathbf{x}_{m,j} \cdot {}^t \mathbf{x}_{b,i}) - ({}^0 \mathbf{x}_{m,i} \cdot {}^0 \mathbf{x}_{b,j} + {}^0 \mathbf{x}_{m,j} \cdot {}^0 \mathbf{x}_{b,i}), \quad (11c)$$

$${}^t \epsilon_{ij}^{b2} = \frac{1}{2} ({}^t \mathbf{x}_{b,i} \cdot {}^t \mathbf{x}_{b,j} + {}^t \mathbf{x}_{b,j} \cdot {}^t \mathbf{x}_{b,i}) - \frac{1}{2} ({}^0 \mathbf{x}_{b,i} \cdot {}^0 \mathbf{x}_{b,j} + {}^0 \mathbf{x}_{b,j} \cdot {}^0 \mathbf{x}_{b,i}), \quad (11d)$$

with

$${}^t \mathbf{x}_{m,i} = \frac{\partial {}^t \mathbf{x}_m}{\partial r_i}, \quad {}^t \mathbf{x}_{b,i} = \frac{\partial {}^t \mathbf{x}_b}{\partial r_i}.$$

In Eq. (11a), the term  ${}^t \epsilon_{ij}^m$  is the covariant in-plane strain at the shell mid-surface ( $\zeta = 0$ ), which in general can induce membrane locking.

In the geometric nonlinear formulation of the MITC4+ shell element, the assumed membrane strain fields are applied based on the current configuration. Hence the covariant membrane strain in Eq. (11b) is considered

$${}^t \epsilon_{ij}^m = \frac{1}{2} {}^t g_{ij}^m - \frac{1}{2} {}^0 g_{ij}^m \quad \text{with } i, j = 1, 2, \quad (12a)$$

with

$${}^t g_{ij}^m = {}^t \mathbf{x}_{m,i} \cdot {}^t \mathbf{x}_{m,j} + {}^t \mathbf{x}_{m,j} \cdot {}^t \mathbf{x}_{m,i}, \quad (12b)$$

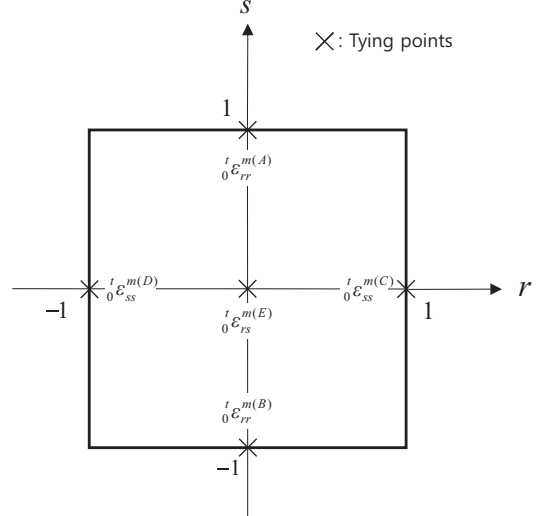


**Fig. 4.** Tying positions (A), (B), (C), (D) and (E) for the assumed membrane strain field.

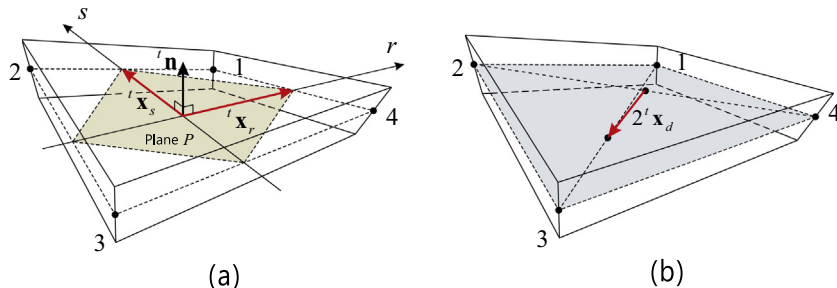


**Fig. 3.** Characteristic vectors for the element geometry at time  $t$ . (a) Two in-plane vectors  ${}^t \mathbf{x}_r$  and  ${}^t \mathbf{x}_s$ , and the plane  $P$  with normal vector  ${}^t \mathbf{n}$ . (b) Distortion vector  ${}^t \mathbf{x}_d$ .

$${}^0g_{ij}^m = {}^0\mathbf{x}_{m,i} \cdot {}^0\mathbf{x}_{m,j} + {}^0\mathbf{x}_{m,j} \cdot {}^0\mathbf{x}_{m,i}. \quad (12c)$$

We next define the three characteristic vectors in the configuration at time  $t$  [1]

$${}^t\mathbf{x}_r = \frac{1}{4} \sum_{i=1}^4 \xi_i {}^t\mathbf{x}_i, \quad {}^t\mathbf{x}_s = \frac{1}{4} \sum_{i=1}^4 \eta_i {}^t\mathbf{x}_i, \quad {}^t\mathbf{x}_d = \frac{1}{4} \sum_{i=1}^4 \xi_i \eta_i {}^t\mathbf{x}_i, \quad (13)$$

in which  $\xi_i$  and  $\eta_i$  are given in Eq. (2). The geometric representations of the three vectors at time  $t$  are shown in Fig. 3.

As shown in Fig. 3(a), the two vectors  ${}^t\mathbf{x}_r$  and  ${}^t\mathbf{x}_s$  form the plane  $P$  with the normal vector  ${}^t\mathbf{n}$

$${}^t\mathbf{n} = \frac{{}^t\mathbf{x}_r \times {}^t\mathbf{x}_s}{\|{}^t\mathbf{x}_r \times {}^t\mathbf{x}_s\|}, \quad (14)$$

and the dual base vectors  ${}^t\mathbf{m}^r$  and  ${}^t\mathbf{m}^s$  on the plane

$${}^t\mathbf{m}^{ri} \cdot {}^t\mathbf{x}_{rj} = \delta_j^i, \quad {}^t\mathbf{m}^{ri} \cdot {}^t\mathbf{n} = 0 \quad \text{with } i, j = 1, 2.$$

For the MITEC4+ shell element, the following assumed field is used for the covariant membrane strain [1]

$${}^0\tilde{\epsilon}_{ij}^m = \frac{1}{2} {}^t\tilde{g}_{ij}^m - \frac{1}{2} {}^0\tilde{g}_{ij}^m \quad \text{with } i, j = 1, 2 \quad (15a)$$

where

$$\begin{aligned} {}^t\tilde{g}_{rr}^m &= \frac{1}{2} (1 - 2{}^ta_A + s + 2{}^ta_A \cdot s^2) {}^tg_{rr}^{m(A)} \\ &+ \frac{1}{2} (1 - 2{}^ta_B - s + 2{}^ta_B \cdot s^2) {}^tg_{rr}^{m(B)} \\ &+ {}^ta_C (-1 + s^2) {}^tg_{ss}^{m(C)} + {}^ta_D (-1 + s^2) {}^tg_{ss}^{m(D)} \\ &+ {}^ta_E (-1 + s^2) {}^tg_{rs}^{m(E)}, \end{aligned} \quad (15b)$$

$$\begin{aligned} {}^t\tilde{g}_{ss}^m &= {}^ta_A (-1 + r^2) {}^tg_{rr}^{m(A)} + {}^ta_B (-1 + r^2) {}^tg_{rr}^{m(B)} \\ &+ \frac{1}{2} (1 - 2{}^ta_C + r + 2{}^ta_C \cdot r^2) {}^tg_{ss}^{m(C)} \\ &+ \frac{1}{2} (1 - 2{}^ta_D - r + 2{}^ta_D \cdot r^2) {}^tg_{ss}^{m(D)} \\ &+ {}^ta_E (-1 + r^2) {}^tg_{rs}^{m(E)}, \end{aligned} \quad (15c)$$

$$\begin{aligned} {}^t\tilde{g}_{rs}^m &= \frac{1}{4} (r + 4{}^ta_A \cdot rs) {}^tg_{rr}^{m(A)} + \frac{1}{4} (-r + 4{}^ta_B \cdot rs) {}^tg_{rr}^{m(B)} \\ &+ \frac{1}{4} (s + 4{}^ta_C \cdot rs) {}^tg_{ss}^{m(C)} + \frac{1}{4} (-s + 4{}^ta_D \cdot rs) {}^tg_{ss}^{m(D)} \\ &+ (1 + {}^ta_E \cdot rs) {}^tg_{rs}^{m(E)}, \end{aligned} \quad (15d)$$

in which the tying positions (A), (B), (C), (D) and (E) for the corresponding strain components are shown in Fig. 4, and the geometric coefficients are

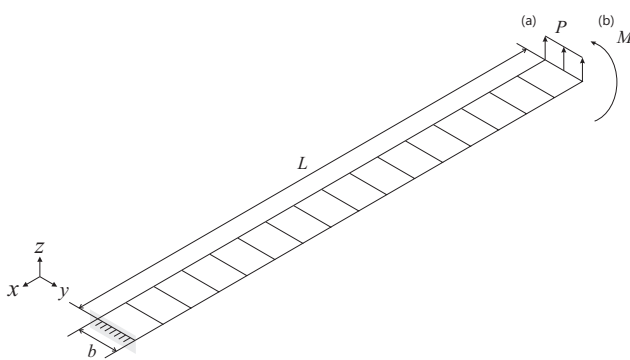


**Fig. 5.** Cantilever problems ( $16 \times 1$  mesh, width  $b = 1.0$ , thickness  $a = 0.1$ ,  $E = 1.2 \times 10^6$  and  $v = 0.0$ ). (a) Case of the tip shearing force ( $L = 10.0$ ). (b) Case of the tip moment ( $L = 12.0$ ).

$$\begin{aligned} {}^ta_A &= \frac{{}^tc_r({}^tc_r - 1)}{2^td}, & {}^ta_B &= \frac{{}^tc_r({}^tc_r + 1)}{2^td}, \\ {}^ta_C &= \frac{{}^tc_s({}^tc_s - 1)}{2^td}, & {}^ta_D &= \frac{{}^tc_s({}^tc_s + 1)}{2^td}, \end{aligned}$$

$${}^ta_E = \frac{2{}^tc_r{}^tc_s}{{}^td}, \quad {}^td = {}^tc_r^2 + {}^tc_s^2 - 1, \quad {}^tc_r = {}^t\mathbf{m}^r \cdot {}^t\mathbf{x}_d, \quad {}^tc_s = {}^t\mathbf{m}^s \cdot {}^t\mathbf{x}_d. \quad (15e)$$

Using the assumed membrane strain fields, the in-plane strain components are constructed

$${}^0\tilde{\epsilon}_{ij} = {}^0\tilde{\epsilon}_{ij}^m + \zeta_0^t \epsilon_{ij}^{b1} + \zeta_0^2 t \epsilon_{ij}^{b2} \quad \text{with } i, j = 1, 2. \quad (16)$$

The shell-aligned local Cartesian coordinate system in the configuration at time 0 is defined using the unit vectors  ${}^0\mathbf{L}_i$ ,  $i = 1, 2, 3$ ,

$${}^0\mathbf{L}_3 = \frac{{}^0\mathbf{g}_3}{\|{}^0\mathbf{g}_3\|}, \quad {}^0\mathbf{L}_1 = \frac{{}^0\mathbf{g}_2 \times {}^0\mathbf{L}_3}{\|{}^0\mathbf{g}_2 \times {}^0\mathbf{L}_3\|}, \quad {}^0\mathbf{L}_2 = {}^0\mathbf{L}_3 \times {}^0\mathbf{L}_1, \quad (17)$$

and the corresponding local strain components are

$${}^0\bar{\epsilon}_{ij} = {}^0\tilde{\epsilon}_{kl} ({}^0\mathbf{L}_i \cdot {}^0\mathbf{g}^k) ({}^0\mathbf{L}_j \cdot {}^0\mathbf{g}^l) \quad \text{with } {}^0\mathbf{g}_i \cdot {}^0\mathbf{g}^j = \delta_i^j. \quad (18)$$

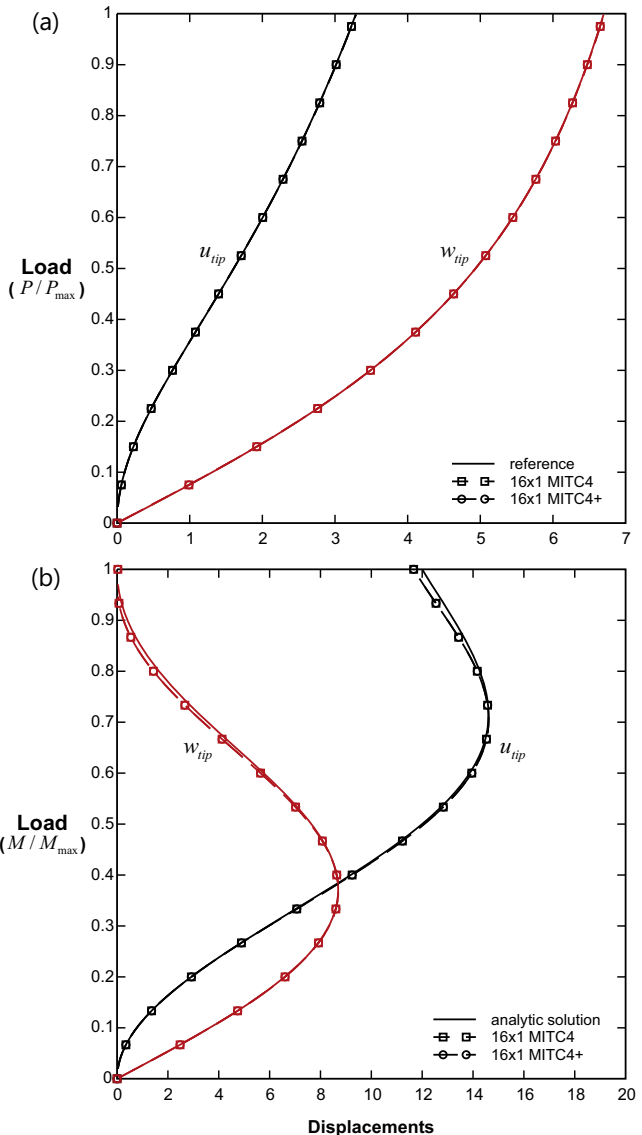


**Fig. 6.** Load-displacement curves for the cantilever. (a) Case of the tip shearing force. (b) Case of the tip moment.

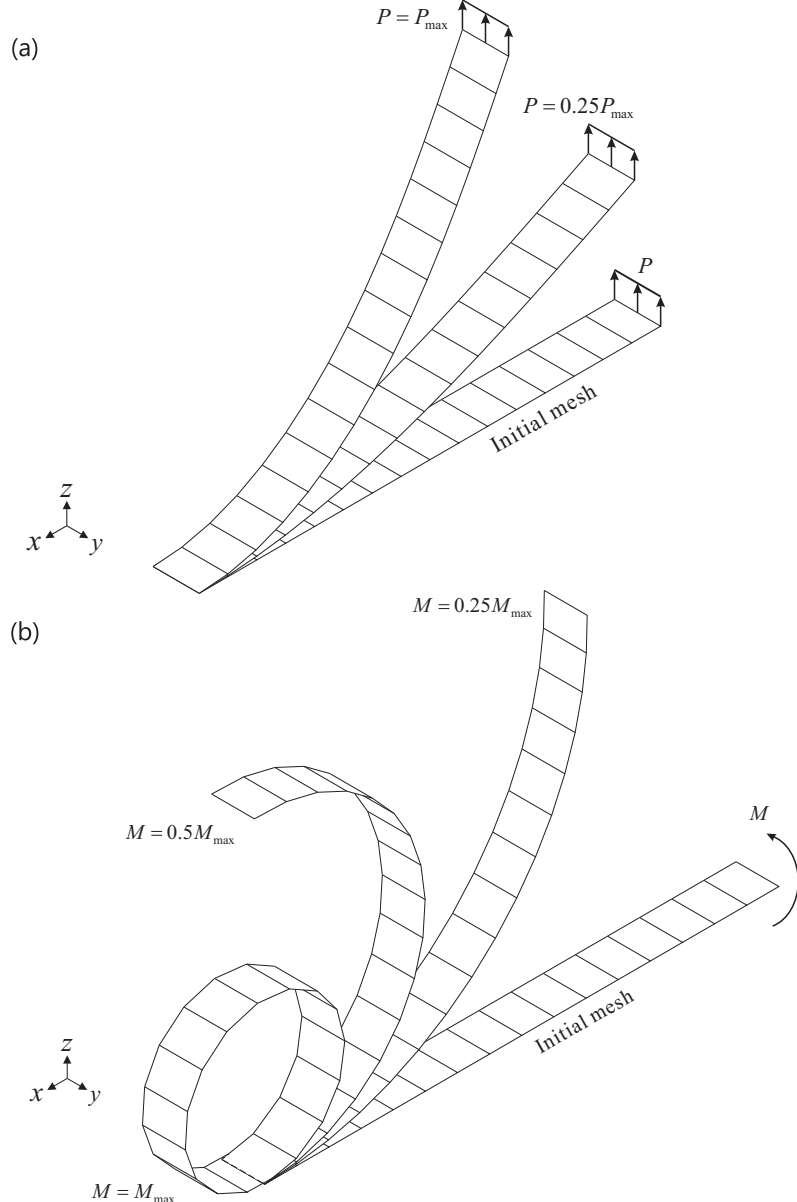


**Fig. 7.** Deformed shapes of the cantilever. (a) Case of the tip shearing force. (b) Case of the tip moment.

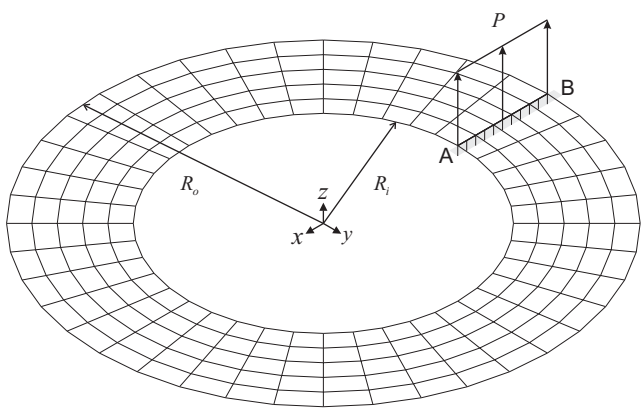


**Fig. 8.** Slit annular plate problem ( $5 \times 40$  mesh,  $R_o = 10.0$ ,  $R_i = 6.0$ , thickness  $a = 0.03$ ,  $E = 2.1 \times 10^7$  and  $\nu = 0.0$ ).

#### 2.4. Assumed incremental Green-Lagrange strains

From the assumed Green-Lagrange strains in Section 2.3, we proceed to obtain the corresponding assumed incremental Green-Lagrange strains in a consistent manner.

For the transverse shear we use the following assumed incremental shear strains

$$\begin{aligned} {}_0\tilde{\epsilon}_{r\xi} &= \frac{1}{2}(1+s)_0\epsilon_{r\xi}^{(A)} + \frac{1}{2}(1-s)_0\epsilon_{r\xi}^{(B)}, \quad {}_0\tilde{\epsilon}_{s\xi} = \frac{1}{2}(1+r)_0\epsilon_{s\xi}^{(C)} + \frac{1}{2}(1-r)_0\epsilon_{s\xi}^{(D)}, \\ {}_0\tilde{\eta}_{r\xi} &= \frac{1}{2}(1+s)_0\eta_{r\xi}^{(A)} + \frac{1}{2}(1-s)_0\eta_{r\xi}^{(B)}, \quad {}_0\tilde{\eta}_{s\xi} = \frac{1}{2}(1+r)_0\eta_{s\xi}^{(C)} + \frac{1}{2}(1-r)_0\eta_{s\xi}^{(D)}, \end{aligned} \quad (19)$$

where the tying positions (A), (B), (C) and (D) are shown in Fig. 2 [1,2,4,8].

The linear and nonlinear parts of the incremental covariant in-plane strains in Eq. (9) are expressed as

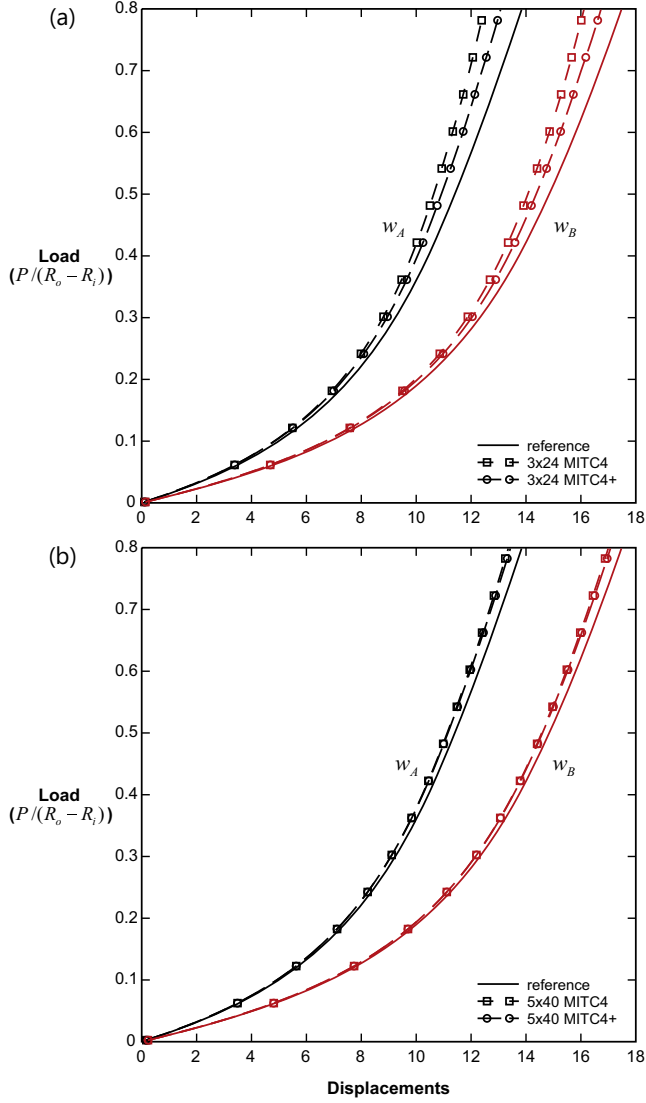


**Fig. 9.** Load-displacement curves for the slit annular plate problem. (a)  $3 \times 24$  mesh. (b)  $5 \times 40$  mesh.

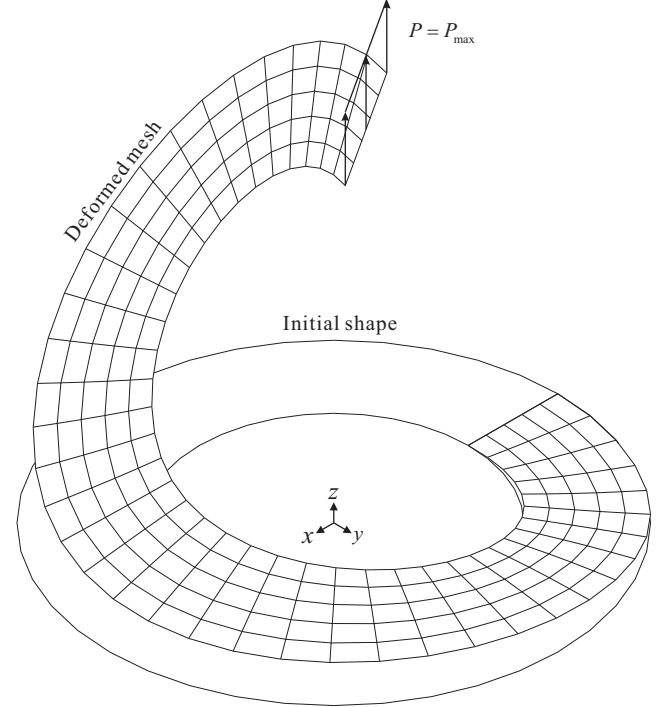


**Fig. 10.** Deformed shape for the slit annular plate problem.

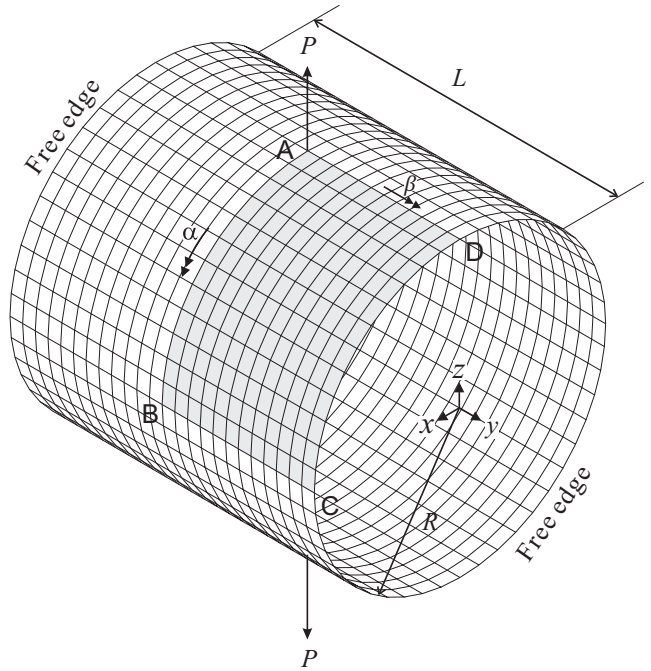


**Fig. 11.** Pull-out of a free cylindrical shell structure ( $12 \times 12$  mesh,  $R = 4.953$ ,  $L = 10.35$ , thickness  $a = 0.094$ ,  $E = 1.05 \times 10^7$  and  $v = 0.3125$ ).

with

$$\begin{aligned} {}^t \mathbf{x}_{m,i} &= \frac{\partial {}^t \mathbf{x}_m}{\partial r_i}, & {}^t \mathbf{x}_{b,i} &= \frac{\partial {}^t \mathbf{x}_b}{\partial r_i}, & \mathbf{u}_{m,i} &= \frac{\partial \mathbf{u}_m}{\partial r_i}, \\ \mathbf{u}_{b1,i} &= \frac{\partial \mathbf{u}_{b1}}{\partial r_i}, & \mathbf{u}_{b2,i} &= \frac{\partial \mathbf{u}_{b2}}{\partial r_i}. \end{aligned}$$

$$\begin{aligned} {}_0 e_{ij}^m &= {}_0 e_{ij}^m + \zeta {}_0 e_{ij}^{b1} + \zeta^2 {}_0 e_{ij}^{b2}, \\ {}_0 \eta_{ij} &= {}_0 \eta_{ij}^m + \zeta {}_0 \eta_{ij}^{b1} + \zeta^2 {}_0 \eta_{ij}^{b2} \quad \text{with } i, j = 1, 2, \end{aligned} \quad (20a)$$

in which

$${}_0 e_{ij}^m = \frac{1}{2} ({}^t \mathbf{x}_{m,i} \cdot \mathbf{u}_{m,j} + {}^t \mathbf{x}_{m,j} \cdot \mathbf{u}_{m,i}), \quad (20b)$$

$${}_0 e_{ij}^{b1} = \frac{1}{2} ({}^t \mathbf{x}_{m,i} \cdot \mathbf{u}_{b1,j} + {}^t \mathbf{x}_{m,j} \cdot \mathbf{u}_{b1,i} + {}^t \mathbf{x}_{b,i} \cdot \mathbf{u}_{m,j} + {}^t \mathbf{x}_{b,j} \cdot \mathbf{u}_{m,i}), \quad (20c)$$

$${}_0 e_{ij}^{b2} = \frac{1}{2} ({}^t \mathbf{x}_{b,i} \cdot \mathbf{u}_{b1,j} + {}^t \mathbf{x}_{b,j} \cdot \mathbf{u}_{b1,i}), \quad (20d)$$

$${}_0 \eta_{ij}^m = \frac{1}{2} \mathbf{u}_{m,i} \cdot \mathbf{u}_{m,j}, \quad (20e)$$

$${}_0 \eta_{ij}^{b1} = \frac{1}{2} (\mathbf{u}_{m,i} \cdot \mathbf{u}_{b1,j} + \mathbf{u}_{m,j} \cdot \mathbf{u}_{b1,i} + {}^t \mathbf{x}_{m,i} \cdot \mathbf{u}_{b2,j} + {}^t \mathbf{x}_{m,j} \cdot \mathbf{u}_{b2,i}), \quad (20f)$$

$${}_0 \eta_{ij}^{b2} = \frac{1}{2} (\mathbf{u}_{b1,i} \cdot \mathbf{u}_{b1,j} + {}^t \mathbf{x}_{b,i} \cdot \mathbf{u}_{b2,j} + {}^t \mathbf{x}_{b,j} \cdot \mathbf{u}_{b2,i}), \quad (20g)$$

In Eq. (20a), the  ${}_0\tilde{e}_{ij}^m$  and  ${}_0\eta_{ij}^m$  terms are the linear and nonlinear incremental covariant in-plane strains at the shell mid-surface ( $\zeta = 0$ ); these in-plane membrane strains can in general induce membrane locking.

From the assumed Green-Lagrange membrane strains in Eq. (15), we derive the assumed incremental linear membrane strain  ${}_0\tilde{e}_{ij}^m$  in Eq. (20b)

$$\begin{aligned} {}_0\tilde{e}_{rr}^m &= \frac{1}{2}(1 - 2^t a_A + s + 2^t a_A \cdot s^2) {}_0e_{rr}^{m(A)} \\ &+ \frac{1}{2}(1 - 2^t a_B - s + 2^t a_B \cdot s^2) {}_0e_{rr}^{m(B)} \\ &+ {}^t a_C(-1 + s^2) {}_0e_{ss}^{m(C)} + {}^t a_D(-1 + s^2) {}_0e_{ss}^{m(D)} \\ &+ {}^t a_E(-1 + s^2) {}_0e_{rs}^{m(E)}, \end{aligned} \quad (21a)$$

$$\begin{aligned} {}_0\tilde{e}_{ss}^m &= {}^t a_A(-1 + r^2) {}_0e_{rr}^{m(A)} + {}^t a_B(-1 + r^2) {}_0e_{rr}^{m(B)} \\ &+ \frac{1}{2}(1 - 2^t a_C + r + 2^t a_C \cdot r^2) {}_0e_{ss}^{m(C)} \\ &+ \frac{1}{2}(1 - 2^t a_D - r + 2^t a_D \cdot r^2) {}_0e_{ss}^{m(D)} + {}^t a_E(-1 + r^2) {}_0e_{rs}^{m(E)}, \end{aligned} \quad (21b)$$

$$\begin{aligned} {}_0\tilde{e}_{rs}^m &= \frac{1}{4}(r + 4^t a_A \cdot rs) {}_0e_{rr}^{m(A)} + \frac{1}{4}(-r + 4^t a_B \cdot rs) {}_0e_{rr}^{m(B)} \\ &+ \frac{1}{4}(s + 4^t a_C \cdot rs) {}_0e_{ss}^{m(C)} + \frac{1}{4}(-s + 4^t a_D \cdot rs) {}_0e_{ss}^{m(D)} \\ &+ (1 + {}^t a_E \cdot rs) {}_0e_{rs}^{m(E)}, \end{aligned} \quad (21c)$$

with the same geometric coefficients as in Eq. (15e) and the tying positions (A), (B), (C), (D) and (E) in Fig. 4.

We employ the same assumed strain field for the incremental nonlinear membrane strain  ${}_0\tilde{\eta}_{ij}^m$ , and hence the incremental in-plane strain components are

$$\begin{aligned} {}_0\tilde{e}_{ij} &= {}_0\tilde{e}_{ij}^m + \zeta {}_0e_{ij}^{b1} + \zeta^2 {}_0e_{ij}^{b2} \text{ and} \\ {}_0\tilde{\eta}_{ij} &= {}_0\tilde{\eta}_{ij}^m + \zeta {}_0\eta_{ij}^{b1} + \zeta^2 {}_0\eta_{ij}^{b2} \quad \text{with } i, j = 1, 2. \end{aligned} \quad (22)$$

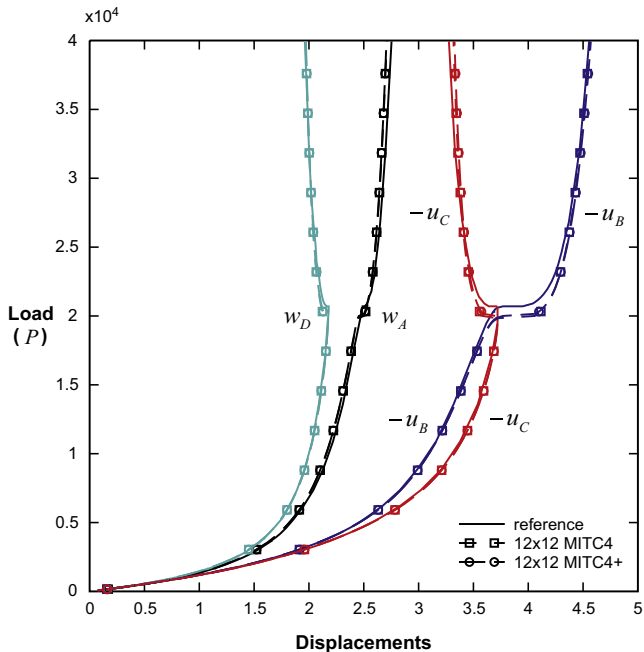


**Fig. 12.** Load-displacement curves for the pull-out of the free cylindrical shell structure.

Using the shell-aligned local Cartesian coordinate system defined in Eq. (17), the linear and nonlinear parts of the incremental local strains are calculated using the following transformations

$$\begin{aligned} {}_0\bar{e}_{ij} &= {}_0\tilde{e}_{kl}({}^0\mathbf{L}_i \cdot {}^0\mathbf{g}^k)({}^0\mathbf{L}_j \cdot {}^0\mathbf{g}^l), \\ {}_0\bar{\eta}_{ij} &= {}_0\tilde{\eta}_{kl}({}^0\mathbf{L}_i \cdot {}^0\mathbf{g}^k)({}^0\mathbf{L}_j \cdot {}^0\mathbf{g}^l) \quad \text{with } {}^0\mathbf{g}_i \cdot {}^0\mathbf{g}^j = \delta_i^j. \end{aligned} \quad (23)$$

## 2.5. Stiffness matrix and internal force vector

Using the standard total Lagrangian formulation [4,18,31], the tangent stiffness matrix ( ${}^t\mathbf{K}_e$ ) and internal force vector ( ${}^t\mathbf{F}_e$ ) of the MITC4+ shell element are obtained

$${}^t\mathbf{K}_e = \int_{0V} \mathbf{B}_{ij}^T \bar{C}_{ijkl} \mathbf{B}_{kl} d^0V + \int_{0V} {}^t\bar{S}_{ij} \mathbf{N}_{ij} d^0V, \quad (24a)$$

$${}^t\mathbf{F}_e = \int_{0V} \mathbf{B}_{ij}^T \bar{S}_{ij} d^0V, \quad (24b)$$

in which  ${}^0V$  is the volume of the shell element at time 0, and  $\bar{C}_{ijkl}$  and  ${}^t\bar{S}_{ij}$  denote, respectively, the material law tensor and the second Piola-Kirchhoff stress measured in the local Cartesian coordinate system.

In Eq. (24), the strain-displacement matrices,  $\mathbf{B}_{ij}$  and  $\mathbf{N}_{ij}$ , are defined by

$${}_0\bar{e}_{ij} = \mathbf{B}_{ij} \mathbf{U}_e, \quad {}_0\bar{\eta}_{ij} = \delta \mathbf{U}_e^T \mathbf{N}_{ij} \mathbf{U}_e, \quad (25)$$

where  $\mathbf{U}_e$  is the incremental nodal displacement vector

$$\mathbf{U}_e = [\mathbf{U}_1^T \quad \mathbf{U}_2^T \quad \mathbf{U}_3^T \quad \mathbf{U}_4^T]^T \quad \text{with } \mathbf{U}_i = [u_i \quad v_i \quad w_i \quad \alpha_i \quad \beta_i]^T.$$

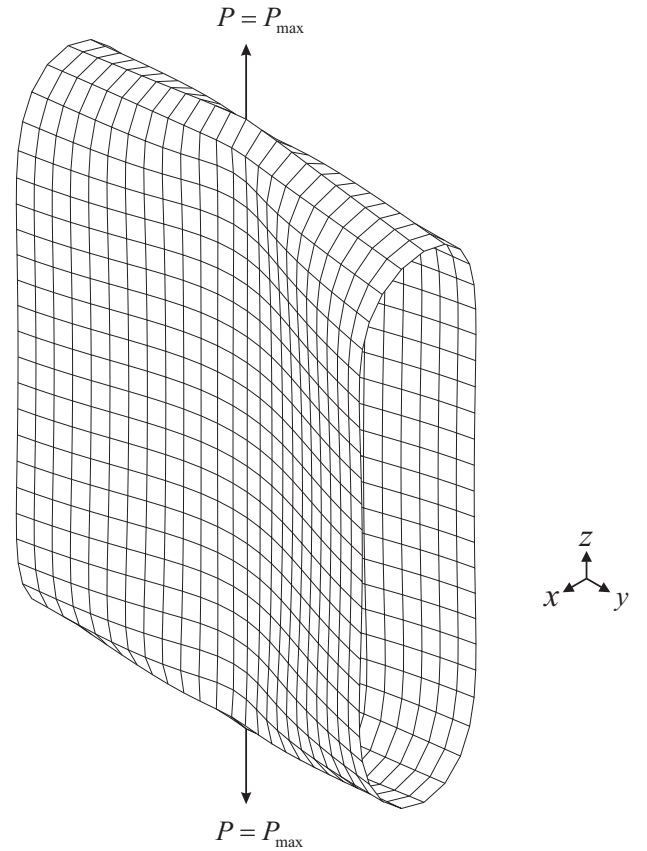


**Fig. 13.** Deformed shape for the pull-out of the free cylindrical shell structure.

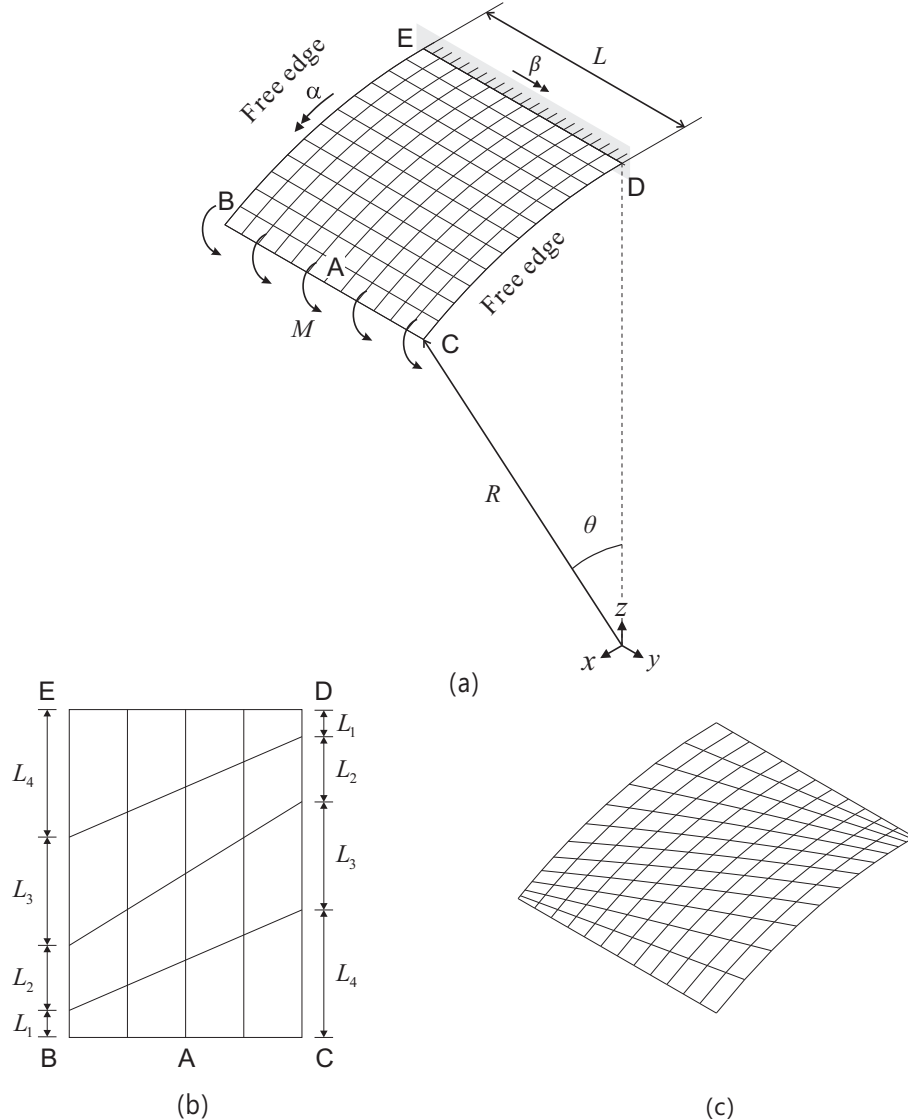


**Fig. 14.** Bending of a cylindrical shell structure ( $R = 10.0$ ,  $\theta = 30^\circ$ ,  $L = 20.0$ , thickness  $a$ ,  $E = 2.1 \times 10^6$  and  $\nu = 0.0$ ). (a) Problem description (12  $\times$  12 uniform mesh). (b) Distorted mesh pattern (4  $\times$  4 mesh). (c) Distorted mesh pattern used (12  $\times$  12 mesh).

In the nonlinear solution procedure, the nodal geometry is updated using Eq. (4b), and the vectors  ${}^t\mathbf{V}_1^i$ ,  ${}^t\mathbf{V}_2^i$  and  ${}^t\mathbf{V}_n^i$  at node  $i$  are updated using the following equations:

$${}^{t+\Delta t}\mathbf{V}_n^i = \mathbf{Q} {}^t\mathbf{V}_n^i, \quad {}^{t+\Delta t}\mathbf{V}_1^i = \mathbf{Q} {}^t\mathbf{V}_1^i, \quad {}^{t+\Delta t}\mathbf{V}_2^i = \mathbf{Q} {}^t\mathbf{V}_2^i, \quad (26)$$

with

$$\mathbf{Q} = 2 \begin{pmatrix} q_0^2 + q_1^2 - \frac{1}{2} & q_1 q_2 - q_0 q_3 & q_3 q_1 + q_0 q_2 \\ q_1 q_2 + q_0 q_3 & q_0^2 + q_2^2 - \frac{1}{2} & q_2 q_3 - q_0 q_1 \\ q_3 q_1 - q_0 q_2 & q_2 q_3 + q_0 q_1 & q_0^2 + q_3^2 - \frac{1}{2} \end{pmatrix},$$

$$q_0 = \cos\left(\frac{\theta_i}{2}\right), \quad [q_1 \quad q_2 \quad q_3]^T = \frac{\boldsymbol{\theta}_i}{\|\boldsymbol{\theta}_i\|} \sin\left(\frac{\theta_i}{2}\right), \quad \theta_i = \|\boldsymbol{\theta}_i\|,$$

in which a quaternion representation of large rotations is utilized [32].

In the finite element solutions, we use  $2 \times 2 \times 2$  Gauss integration over the element volume for the 4-node shell elements considered. The computational cost of the MITC4+ shell element

is only slightly higher than the cost of the classical MITC4 shell element due to the use of the assumed covariant membrane strains.

### 3. Numerical examples

In this section, several numerical examples are solved to demonstrate the performance of the MITC4+ shell element in geometric nonlinear analysis. The results are compared with those obtained using of the classical MITC4 shell element. The reference solutions are analytical data or are obtained using a fine uniform mesh of the MITC9 shell element, which is known to satisfy the ellipticity and consistency conditions and to show good convergence behavior in both linear and nonlinear analyses [4–8,17–20].

We show in the example solutions that both the MITC4 and MITC4+ elements work well when uniform meshes are used and due to the specific physical problem the large displacements of the meshes do not induce locking, but in contrast to the MITC4

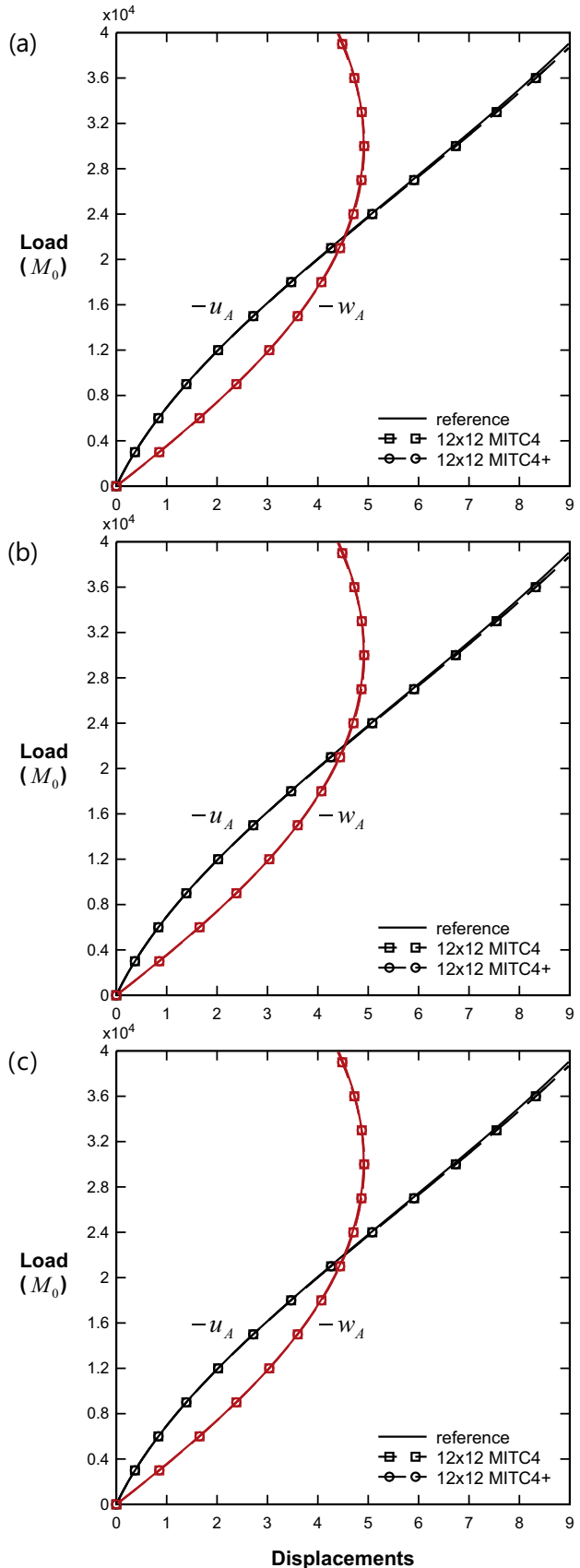


**Fig. 15.** Load-displacement curves for the bending of the cylindrical shell structure with the uniform mesh. (a)  $a/R = 1/100$ . (b)  $a/R = 1/1000$ . (c)  $a/R = 1/10,000$ .

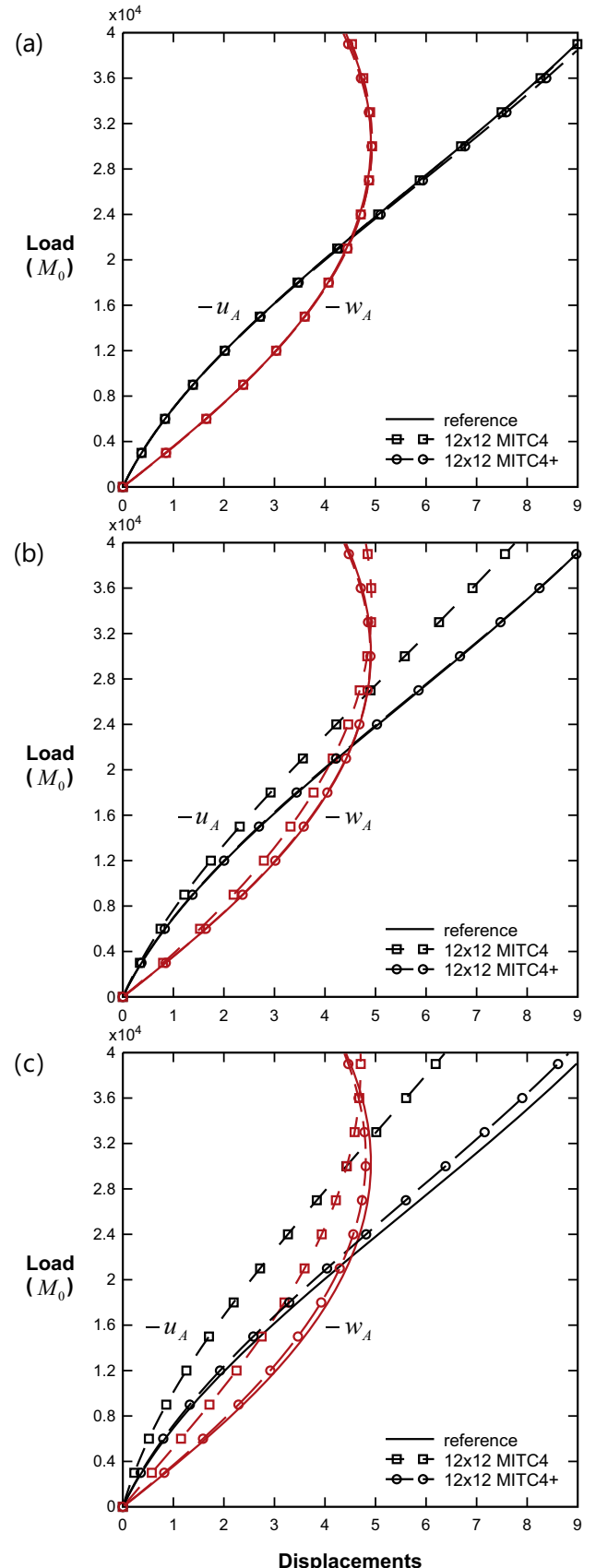


**Fig. 16.** Load-displacement curves for the bending of the cylindrical shell structure with the distorted mesh. (a)  $a/R = 1/100$ . (b)  $a/R = 1/1000$ . (c)  $a/R = 1/10,000$ .

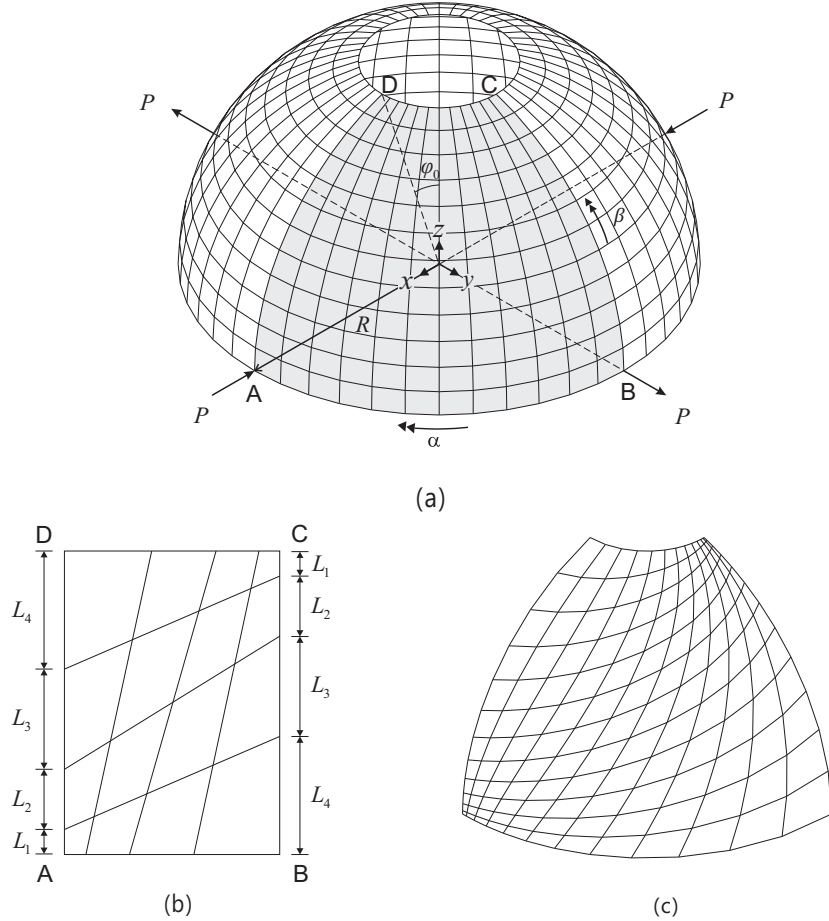


**Fig. 17.** Hemispherical shell problem ( $R = 10.0$ ,  $\varphi_0 = 18^\circ$ , thickness  $a = 0.04$ ,  $E = 6.825 \times 10^7$  and  $v = 0.3$ ). (a) Problem description (12  $\times$  12 uniform mesh). (b) Distorted mesh pattern (4  $\times$  4 mesh). (c) Distorted mesh pattern applied (12  $\times$  12 mesh).

shell element, the MITC4+ element also works well when an initially distorted mesh is used for such problem solutions, see Sections 3.1–3.4.

We also show the important point that the MITC4+ element is more effective than the MITC4 element in response solutions when due to the physical nature of the shell problem an initially uniform mesh in the large displacement response can induce locking. In this case, the MITC4 element locks in membrane actions whereas the MITC4+ element continues to work well, see Sections 3.5–3.7.

### 3.1. Cantilever problem

We consider the cantilever bending problem in Fig. 5 [11–13,33]. The cantilever fully clamped at one end is subjected to either a shearing force  $P$  or bending moment  $M$  at the free tip. The cantilever is modeled with a  $16 \times 1$  mesh for the MITC4 and MITC4+ shell elements.

For the shearing load case, the reference solution is obtained using a  $32 \times 1$  mesh of MITC9 shell elements. We consider the maximum load of  $P_{\max} = 4P_0$  with  $P_0 = EI/L$  and  $I = ba^3/12$ .

For the moment load case, the cantilever develops to form a circular arc of radius  $R = EI/M$  with  $I = ba^3/12$ . Using this formula, the following analytical tip displacements are obtained [12,13]

$$\frac{u_{\text{tip}}}{L} = \frac{M_0}{M} \sin \frac{M}{M_0} - 1, \quad \frac{w_{\text{tip}}}{L} = \frac{M_0}{M} \left( 1 - \cos \frac{M}{M_0} \right), \quad M_0 = \frac{EI}{L}. \quad (27)$$

The cantilever beam should bend into a complete circle at the applied tip moment  $M_{\max} = 2\pi M_0$ .

Fig. 6 shows the load-displacement curves of the MITC4 and MITC4+ shell elements. The solutions using both elements agree well with the reference and analytic solutions. Fig. 7 shows the deformed shapes at successive load levels  $P/P_{\max} = 0.25$  and 1.0 for the shearing load case and  $M/M_{\max} = 0.25, 0.5$  and 1.0 for the moment load case.

### 3.2. Slit annular plate problem

We next consider the slit annular plate problem shown in Fig. 8 [12,13,15,34]. The shearing force  $P$  is applied at one end of the slit while the other end is fully clamped. We use  $3 \times 24$  and  $5 \times 40$  meshes for the MITC4 and MITC4+ shell elements. The maximum load per unit length  $P_{\max}/(R_o - R_i) = 0.8$  is considered. The reference solution is obtained using a  $10 \times 80$  mesh of MITC9 shell elements. Fig. 9 shows the load-displacement curves. The solution obtained using the MITC4+ shell element is slightly better than the solution using the MITC4 shell element. The final deformed shape of the structure calculated using the MITC4+ shell element is presented in Fig. 10.

### 3.3. Pull-out of a free cylindrical shell

We consider a pull-out of the free cylindrical shell structure shown in Fig. 11 [12,13,34]. The shell structure is subjected to a

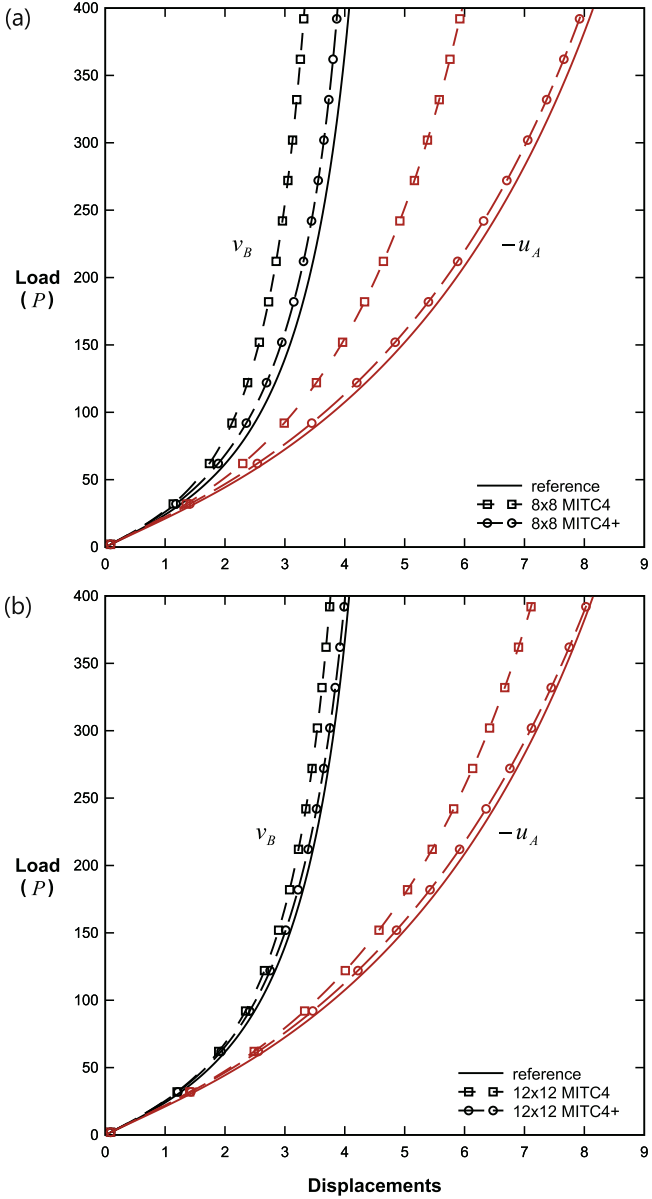


**Fig. 18.** Load-displacement curves for the hemispherical shell problem with the uniform mesh shown in Fig. 8(a). (a)  $8 \times 8$  mesh. (b)  $12 \times 12$  mesh.

pair of pull-out loads ( $P$ ) at its center. Due to symmetry, only one-eighth of the structure corresponding to the shaded region ABCD in Fig. 11 is modeled using a  $12 \times 12$  mesh of the 4-node shell elements. We use the following boundary conditions:  $w = \beta = 0$  along BC,  $u = \beta = 0$  along AD, and  $v = \alpha = 0$  along AB. The analysis is performed up to  $P_{\max} = 4 \times 10^4$ . The reference solutions are obtained using a  $32 \times 32$  mesh of MITC9 shell elements. Fig. 12 shows the resulting load-displacement curves. The MITC4 and MITC4+ shell elements perform very well. Fig. 13 presents the final deformed shape of the structure obtained using the MITC4+ shell element.

#### 3.4. Bending of a cylindrical shell structure

We solve the bending problem of a cylindrical shell structure shown in Fig. 14(a) [11,16–18]. The structure is subjected to uniform bending moment  $M$  along BC. Three thickness to radius ratios,  $a/R = 1/100$ ,  $a/R = 1/1000$  and  $a/R = 1/10,000$ , are considered. The applied moment varies with the thickness  $a$  considered

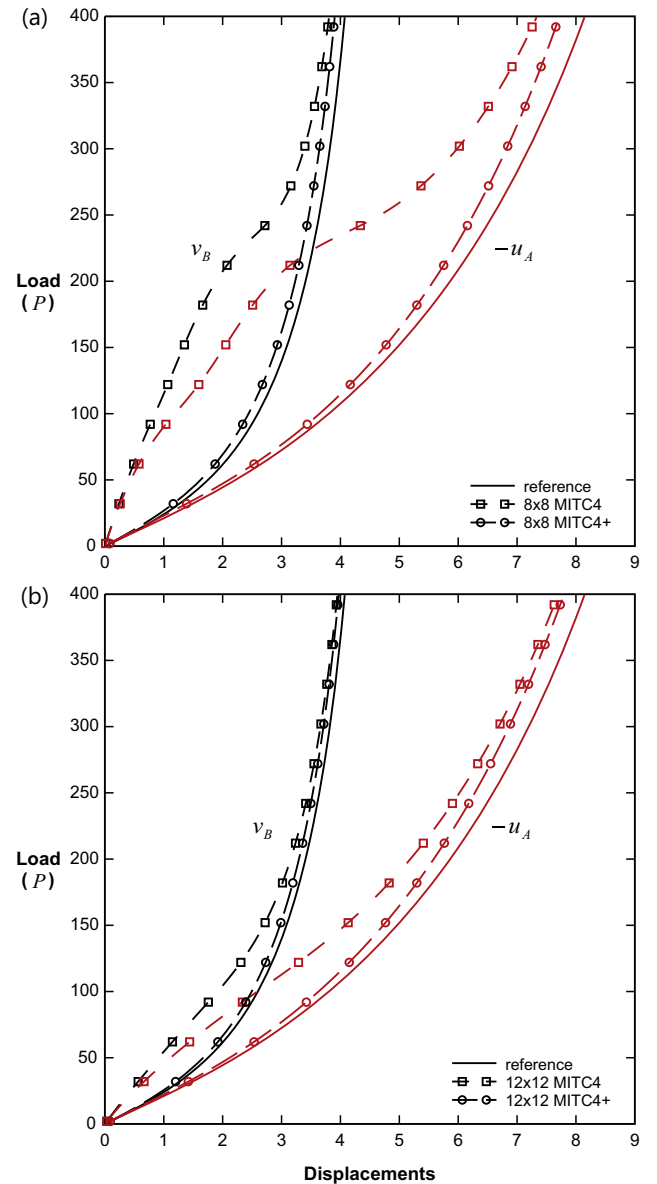


**Fig. 19.** Load-displacement curves for the hemispherical shell problem with the distorted mesh shown in Fig. 8(c). (a)  $8 \times 8$  mesh. (b)  $12 \times 12$  mesh.

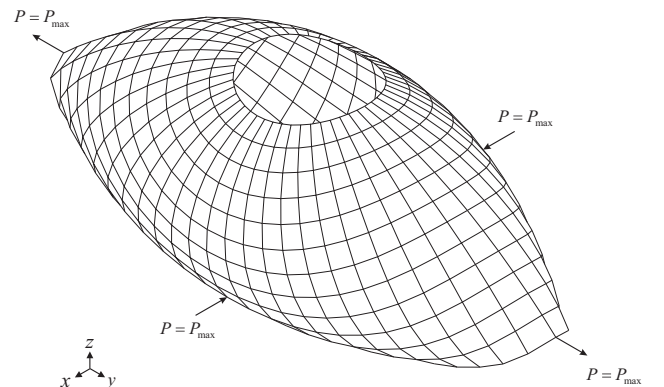


**Fig. 20.** Deformed shape of the hemispherical shell ( $12 \times 12$  uniform mesh used).

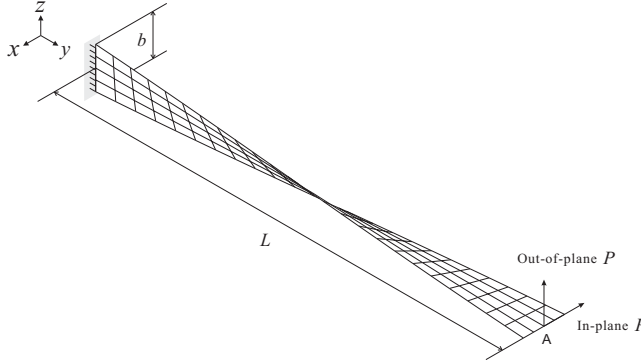


**Fig. 21.** Twisted cantilever beam problems ( $4 \times 24$  mesh,  $L = 12.0$ ,  $b = 1.1$ , thickness  $a = 0.0032$ ,  $E = 2.9 \times 10^7$  and  $\nu = 0.22$ ).

according to  $M = M_0 a^3$ . A fully clamped boundary condition is applied,  $u = v = w = \alpha = \beta = 0$  along DE. For each thickness, we consider the load level up to  $(M_0)_{\max} = 4.0 \times 10^4$ .

In addition to the uniform mesh in Fig. 14(a), we also consider the distorted mesh pattern shown in Fig. 14(b). For an  $N \times N$  element mesh, a pair of edges are discretized in the following ratio:  $L_1 : L_2 : L_3 : \dots : L_N = 1 : 2 : 3 : \dots : N$ . The distorted mesh is shown in Fig. 14(c). For the 4-node shell elements a  $12 \times 12$  mesh is used. A  $32 \times 32$  mesh of MITC9 shell elements is employed to obtain the reference solution.

Fig. 15 shows the load-displacement curves for the uniform mesh, where the solutions obtained using the MITC4 and MITC4+ shell elements agree well with the reference solution. Fig. 16 shows the load-displacement curves when the distorted mesh is used. As the shell thickness decreases, the solutions obtained using the MITC4 shell element depart from the reference solution. However, using the MITC4+ shell element good response predictions are always obtained.

### 3.5. Hemispherical shell problem

We solve the hemispherical shell problem shown in Fig. 17(a) [13–15,17,18,34]. The hemispherical shell with an  $18^\circ$  cutout at its pole is subjected to alternating radial point forces ( $P$ ) at its equator. In this bending problem, the shell structure undergoes almost inextensional deformations and thus we test whether membrane locking occurs. Due to symmetry, only one quarter of the structure corresponding to the shaded region ABCD in Fig. 17(a) is modeled using uniform meshes of  $8 \times 8$  and  $12 \times 12$  4-node shell elements. We use the following boundary conditions:  $u = \beta = 0$  along BC,  $v = \beta = 0$  along AD, and  $w = 0$  at A. The maximum load of  $P_{\max} = 400$  is considered.

In addition to the uniform mesh in Fig. 17(a), we consider the distorted mesh pattern shown in Fig. 17(b) in which we use an  $N \times N$  element mesh, each edge is discretized in the following ratio:  $L_1 : L_2 : L_3 : \dots : L_N = 1 : 2 : 3 : \dots : N$ . The distorted mesh in one quarter of the hemisphere is shown in Fig. 17(c). To obtain the reference solution, a  $32 \times 32$  uniform mesh of MITC9 shell elements is employed.

Figs. 18 and 19 present the load-displacement curves for the uniform and distorted meshes, respectively. As the mesh is refined, the solutions obtained using the MITC4+ shell element converge to the reference solution more rapidly than those obtained with the MITC4 shell element. For the distorted mesh cases, the MITC4 shell element gives a response with a large error from the reference solution. However, the MITC4+ shell element still shows a good behavior. Fig. 20 gives the final deformed shape of the hemispherical shell calculated using the MITC4+ shell element.

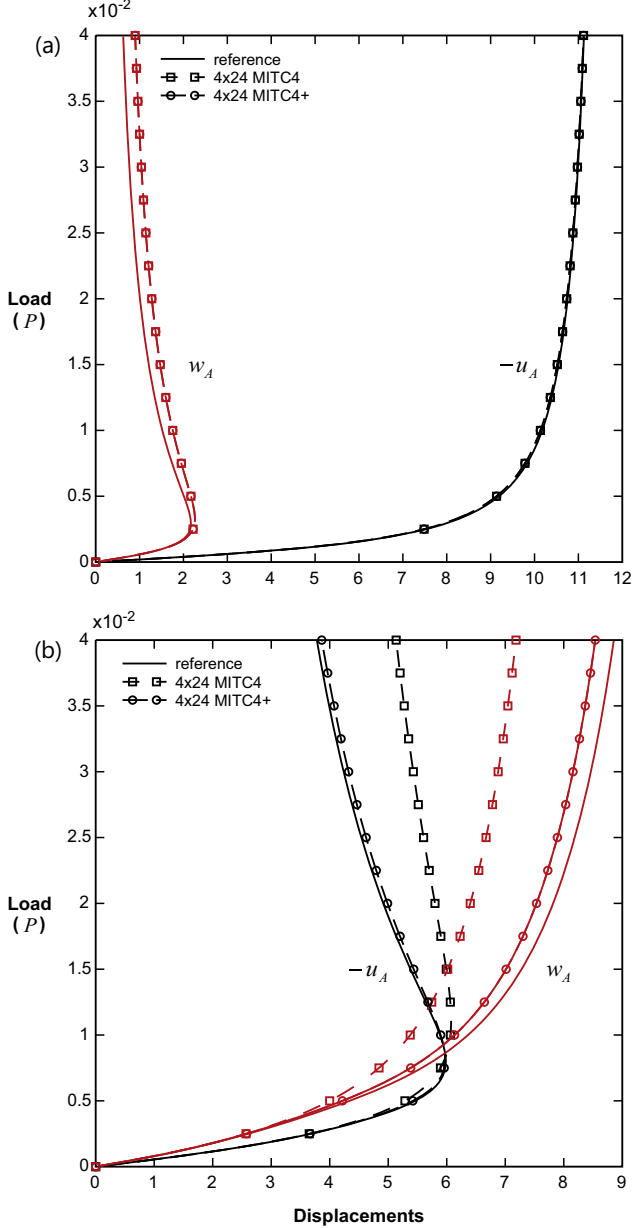


**Fig. 22.** Load-displacement curves for the twisted cantilever beam problem. (a) Case of the in-plane load. (b) Case of the out-of-plane load.

### 3.6. Twisted cantilever beam problems

We consider the twisted cantilever beam problems shown in Fig. 21 [26,34,35]. The initially twisted beam is fully clamped at one end and is loaded by a point load  $P$  at the center of the free tip. Two load cases are considered: an in-plane and an out-of-plane load as shown in Fig. 21. We use a  $4 \times 24$  mesh of the 4-node elements while an  $8 \times 48$  mesh of MITC9 shell elements is used for the reference solutions. The maximum load level is  $P_{\max} = 4 \times 10^{-2}$  for both load cases.

Fig. 22 gives the load-displacement curves for both the in-plane and out-of-plane loads. No severe locking is present for the in-plane load case, where both 4-node shell elements perform well. When the out-of-plane load is applied, the response predicted using the MITC4 shell element deviates significantly from the reference solution due to membrane locking. However, the MITC4+

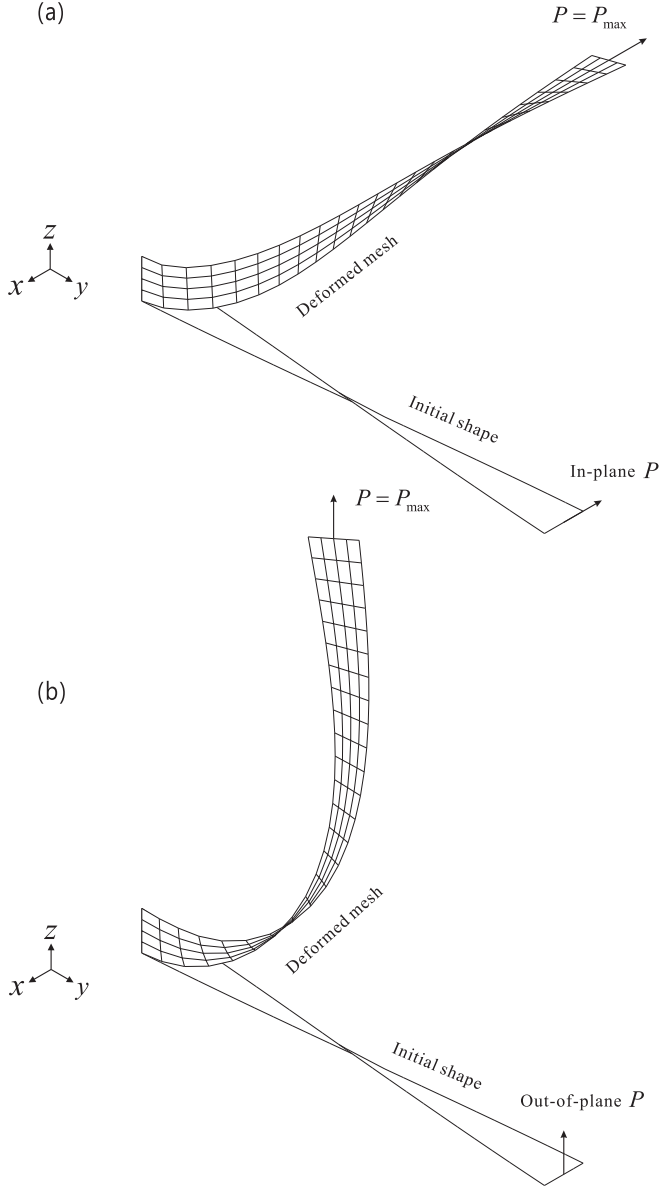


**Fig. 23.** Deformed shapes of the cantilever beam. (a) Case of the in-plane load. (b) Case of the out-of-plane load.

shell element shows a good predictive capability. The final deformed shapes of the cantilever beam obtained using the MITC4+ shell element are presented in Fig. 23.

### 3.7. Hook problem

Finally, we consider the hook problem shown in Fig. 24, referred to in linear analysis as the Raasch challenge, see Ref. [36]. The structure is fully clamped at one end and is loaded by a shear load  $P$  applied as a uniformly distributed traction at the free tip. For the solution, we use a  $4 \times 20$  mesh with the MITC4 and MITC4+ shell elements and an  $8 \times 40$  mesh of MITC9 shell elements to obtain the reference solution. The load is applied up to  $P_{\max} = 1.0 \times 10^{-4}$ . Fig. 25 shows the resulting load-displacement curves. Using the MITC4+ shell element produces a significantly

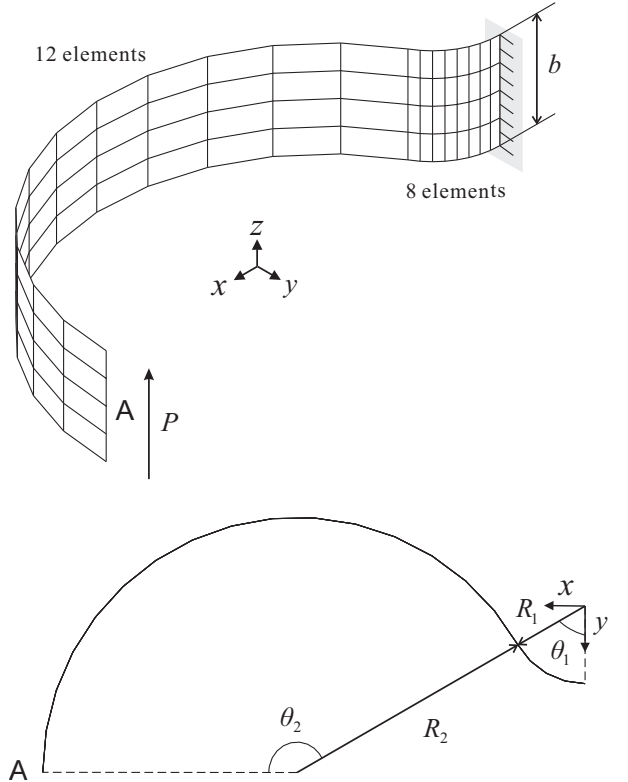


**Fig. 24.** Hook problem ( $4 \times 20$  mesh,  $R_1 = 14$ ,  $\theta_1 = 60^\circ$ ,  $R_2 = 46$ ,  $\theta_2 = 150^\circ$ ,  $b = 20$ , thickness  $a = 0.02$ ,  $E = 3.3 \times 10^3$  and  $v = 0.3$ ).

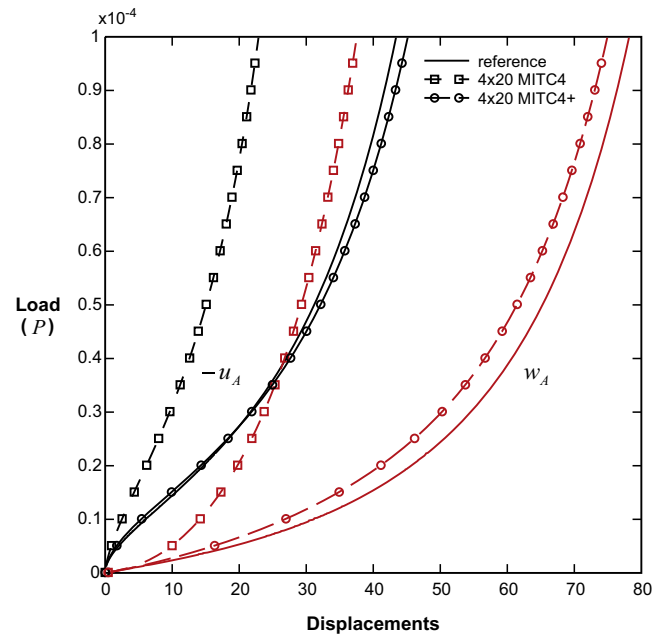


**Fig. 25.** Load-displacement curves for the hook problem.

more accurate solution than using the MITC4 shell element. The final deformed shape of the hook obtained using the MITC4+ shell element is shown in Fig. 26.

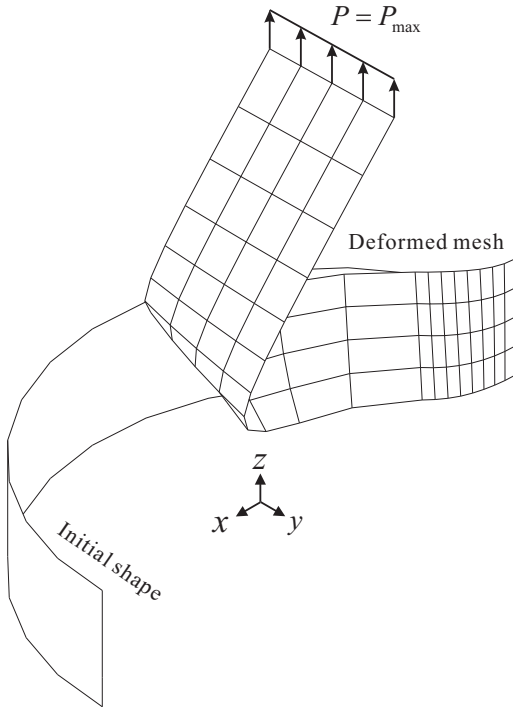


Fig. 26. Deformed shape of the hook.

#### 4. Concluding remarks

We presented the geometric nonlinear formulation of the MITC4+ continuum mechanics-based shell element which is formulated using the MITE approach to alleviate shear and membrane locking. The assumed shear and membrane strain fields used in linear analysis are developed for geometric nonlinear analysis in a consistent manner. The nonlinear performance of the MITC4+ shell element is numerically tested through the solutions of various examples. The computational cost of the element is only slightly higher than the cost of the classical MITC4 shell element.

We can conclude that the MITC4+ shell element provides reliable and efficient solutions in large displacement problems. Compared to the original MITC4 element, the MITC4+ shell element shows improved performance when distorted meshes in the initial configuration are used. Moreover, the MITC4+ element performs much better than the MITC4 shell element when due to the nature of the shell problem, the large displacements of the mesh can induce locking. Hence, we can conclude that the MITC4+ shell element shows excellent behavior in both linear and nonlinear analyses.

#### Acknowledgments

This work was supported by the Basic Science Research Program through the National Research Foundation of Korea funded by the Ministry of Science, ICT, and Future Planning (No. 2014R1A1A1A05007219), and a grant (MPSS-CG-2016-04) through the Disaster and Safety Management Institute funded by Ministry of Public Safety and Security of Korean government.

#### References

- [1] Ko Y, Lee PS, Bathe KJ. A new MITC4+ shell element. Comput Struct 2017;182:404–18.

- [2] Dvorkin EN, Bathe KJ. A continuum mechanics based four-node shell element for general nonlinear analysis. Eng Comput 1984;1(1):77–88.
- [3] Bathe KJ. The finite element method. In: Wahl B, editor. Encyclopedia of computer science and engineering. John Wiley and Sons; 2009. p. 1253–64.
- [4] Bathe KJ. Finite element procedures. Prentice Hall; 1996, 2nd edition KJ Bathe, Watertown, MA; 2014 and Higher Education Press, China, 2016.
- [5] Bathe KJ. The inf-sup condition and its evaluation for mixed finite element methods. Comput Struct 2001;79(2):243–52.
- [6] Bathe KJ, Iosilevich A, Chapelle D. An inf-sup test for shell finite elements. Comput Struct 2000;75(5):439–56.
- [7] Bathe KJ, Lee PS. Measuring the convergence behavior of shell analysis schemes. Comput Struct 2011;89(3):285–301.
- [8] Chapelle D, Bathe KJ. The finite element analysis of shells – fundamentals. 2nd ed. Berlin: Springer; 2003. p. 2011.
- [9] Chapelle D, Bathe KJ. Fundamental considerations for the finite element analysis of shell structures. Comput Struct 1998;66(1):19–36, 711–2.
- [10] Lee PS, Bathe KJ. On the asymptotic behavior of shell structures and the evaluation in finite element solutions. Comput Struct 2002;80(3):235–55.
- [11] Bathe KJ, Dvorkin E, Ho LW. Our discrete-Kirchhoff and isoparametric shell elements for nonlinear analysis – an assessment. Comput Struct 1983;16(1):89–98.
- [12] Arciniega RA, Reddy JN. Tensor-based finite element formulation for geometrically nonlinear analysis of shell structures. Comput Meth Appl Mech Eng 2007;196(4):1048–73.
- [13] Sze KY, Liu XH, Lo SH. Popular benchmark problems for geometric nonlinear analysis of shells. Finite Elem Anal Des 2004;40(11):1551–69.
- [14] Klinkel S, Gruttmann F, Wagner W. A robust non-linear solid shell element based on a mixed variational formulation. Comp Meth App Mech Eng 2006;195(1):179–201.
- [15] Jeon HM, Lee Y, Lee PS, Bathe KJ. The MITC3+ shell element in geometric nonlinear analysis. Comput Struct 2015;146:91–104.
- [16] Bathe KJ, Dvorkin EN. A formulation of general shell elements - the use of mixed formulation of tensorial components. Int J Numer Meth Eng 1986;22(3):697–722.
- [17] Buccale ML, Bathe KJ. Higher-order MITC general shell elements. Int J Numer Meth Eng 1993;36(21):3729–54.
- [18] Buccale ML, Bathe KJ. Finite element analysis of shell structures. Arch Comput Meth Eng 1997;4(1):3–61.
- [19] Bathe KJ, Lee PS, Hiller JF. Towards improving the MITC9 shell element. Comput Struct 2003;81(8):477–89.
- [20] Lee PS, Bathe KJ. Insight into finite element shell discretizations by use of the “basic shell mathematical model”. Comput Struct 2005;83(1):69–90.
- [21] Lee PS, Bathe KJ. Development of MITC isotropic triangular shell finite elements. Comput Struct 2004;82(11):945–62.
- [22] Lee Y, Yoon K, Lee PS. Improving the MITC3 shell finite element by using the Hellinger-Reissner principle. Comput Struct 2012;110–111:93–106.
- [23] Lee Y, Lee PS, Bathe KJ. The MITC3+ shell element and its performance. Comput Struct 2014;138:12–23.
- [24] Lee PS, Bathe KJ. The quadratic MITC plate and MITC shell elements in plate bending. Adv Eng Soft 2010;41(5):712–28.
- [25] Vampa V. Analysis of in-layer strains in the low order MITC shell element. Latin Am J Solid Struct 2007;4(2):87–102.
- [26] Belytschko T, Leviathan I. Projection schemes for one-point quadrature shell elements. Comp Meth Appl Mech Eng 1994;115(3):277–86.
- [27] Choi CK, Paik JG. An efficient four node degenerated shell element based on the assumed covariant strain. Struct Eng Mech 1994;2(1):17–34.
- [28] Kulikov GM, Plotnikova SV. A family of ANS four-node exact geometry shell elements in general convected curvilinear coordinates. Int J Numer Meth Eng 2010;83(10):1376–406.
- [29] Wall WA, Bischoff M, Ramm E. A deformation dependent stabilization technique, exemplified by EAS elements at large strains. Comput Meth Appl Mech Eng 2000;188(4):859–71.
- [30] Sussman T, Bathe KJ. Spurious modes in geometrically nonlinear small displacement finite elements with incompatible modes. Comput Struct 2014;140:14–22.
- [31] Yoon K, Lee PS. Nonlinear performance of continuum mechanics based beam elements focusing on large twisting behaviors. Comp Meth Appl Mech Eng 2014;281:106–30.
- [32] Greenwood DT. Advanced dynamics. Cambridge University Press; 2006.
- [33] Ko Y, Lee PS. A 6-node triangular solid-shell element for linear and nonlinear analysis. Int J Numer Meth Eng 2017. <http://dx.doi.org/10.1002/nme.5498>.
- [34] Jung WY, Han SC. An 8-node shell element for nonlinear analysis of shells using the refined combination of membrane and shear interpolation functions. Math Prob Eng 2013;2013.
- [35] Belytschko T, Wong BL, Stolarski H. Assumed strain stabilization procedure for the 9-node Lagrange shell element. Int J Numer Meth Eng 1989;28(2):385–414.
- [36] Knight NF. Raasch challenge for shell elements. AIAA J 1997;35(2):375–81.